Atomic-scale imaging of laser-driven electron dynamics in solids

Daria Popova-Gorelova[1,2,3*] and Robin Santra[1,2,3]

[1]Center for Free-Electron Laser Science CFEL, Deutsches Elektronen-Synchrotron DESY, Notkestr. 85, Hamburg, 22607, Germany.
[2]Department of Physics, Universität Hamburg, Notkestr. 9, Hamburg, 22607, Germany.
[3]The Hamburg Centre for Ultrafast Imaging, Universität Hamburg, Luruper Chaussee 149, Hamburg, 22761, Germany.

*Corresponding author(s). E-mail(s): darya.gorelova@uni-hamburg.de;

Abstract

Resolving laser-driven electron dynamics on their natural time and length scales is essential for understanding and controlling light-induced phenomena. Here, we demonstrate how ultrafast x-ray diffraction can access fundamental information on laser-driven electronic motion in solids. We propose a method based on subcycle-resolved x-ray-optical wave mixing that allows for a straightforward reconstruction of key properties of strong-field-induced electron dynamics with atomic spatial resolution. Namely, this technique provides both phases and amplitudes of the spatial Fourier transform of optically-induced charge distributions, their temporal behavior, and the direction of the instantaneous microscopic optically-induced electron current flow. It captures the rich microscopic structures and symmetry features of laser-driven electronic charge and current density distributions.

Introduction

Strong-field excitation by light can be used for various significant processes in solids, such as manipulation of electronic gaps and structure by light [1–12], or generation of high harmonics (HHG) [13, 14]. These phenomena, on the one hand, have a big potential for the development of petahertz electronics [15–18], and, on the other hand, raise many scientific questions about mechanisms behind them [19, 20]. Access

to microscopic properties of laser-driven electron dynamics is necessary for a deeper understanding of strong-field phenomena in solids [15, 21–24]. New advances to generate few- and sub-femtosecond x-ray pulses enable a real-time microscopic view into laser-driven electron dynamics [24–33] that is essential for revealing their mechanisms.

When light interacts with a material, charges rearrange within a unit cell and microscopic electron currents are formed. The widely-used concept that optically-induced charge separation merely gives rise to a dipole moment fails on the atomic scale. Induced charge distributions have a rich structure and various symmetry features [34, 35]. In this article, we develop a method that employs ultrashort nonresonant x-ray pulses to probe in real time charge and electron current distributions within a unit cell of a crystal during the interaction with an optical field. The method benefits from a short wavelength of hard x rays, which provides sufficient spatial resolution to access the microscopic optical response on the atomic scale.

We build on the idea of x-ray-optical wave mixing (XOWM), in which an x-ray and an optical field simultaneously interact with matter leading to sum and difference generation that encodes microscopic optical response [36, 37]. XOWM has been realized in several experiments at free-electron laser facilities [38–40]. Here, we go beyond this concept and suggest a sub-cycle-resolved measurement, in which the duration of an x-ray pulse is shorter than a period of an optical cycle. X-ray diffraction using ultrashort x-ray pulses provides much more information on laser-driven electron dynamics can be provided by a time-unresolved XOWM.

Results and Discussion

We consider an α-quartz crystal driven by a periodic electromagnetic field with a photon energy of 1.2 eV, an intensity of 10^{12} W/cm^2 and polarized along the (1,1,0) direction. We selected α-quartz for illustration of our results, since this material has recently attracted interest in the context of strong-field-light-induced phenomena [41–46]. HHG in α-quartz has been demonstrated for similar driving laser parameters as those considered here [44, 47].

Figures 1(a)–(l) show the first-, second- and third-order microscopic optical response of α-quartz at different phases during an optical cycle calculated with the Floquet-Bloch formalism combined with the density functional theory (DFT) [35]. Namely, oscillations of the electron density and the electron-current density with frequencies ω, 2ω and 3ω in the presence of the optical electric field evolving as $\sin(\omega t)$ are shown. Blue and yellow isosurfaces indicate positively- and negatively-charged regions relative to the field-free electron density of α-quartz. Except for the first-order response, optically-induced charge rearrangements and microscopic electron currents have an nontrivial structure. A charge distribution due to nonlinear response cannot be characterized in terms of microscopic dipoles, and the microscopic currents form complex vortices. Our method provides a tool to reconstruct these complex structures.

In the following, we consider that an α-quartz crystal is probed by an ultrashort x-ray pulse during the time it is driven by the optical field. In Ref. [48], we developed a general formalism to describe the interaction of an electronic system simultaneously with an optical field and x-ray pulse, and applied it to a description of a

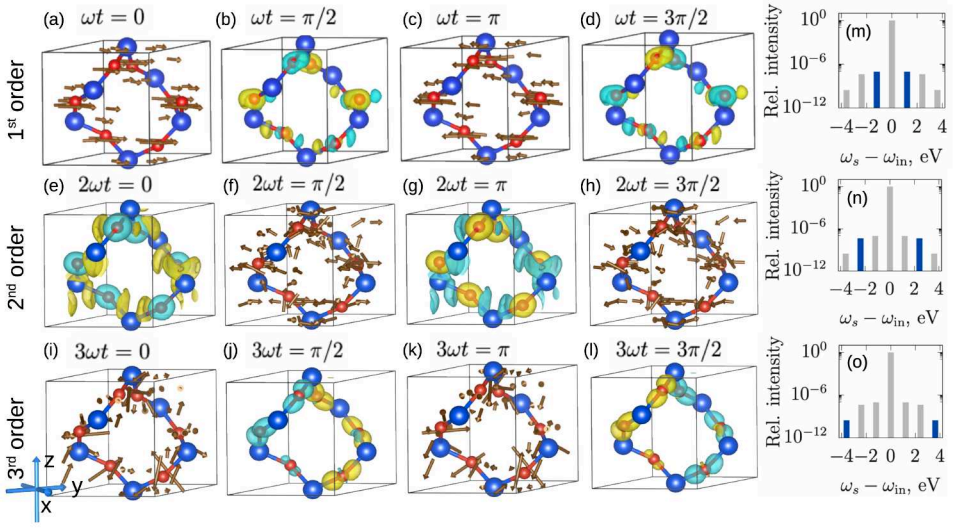

Fig. 1 The first-, second, and third-order microscopic optical response of an α-quartz crystal at different phases of the driving electromagnetic field polarized along the $(1,1,0)$ direction and the corresponding XOWM signal, in which side peaks that appear due to an optical response of the related order are highlighted. A primitive unit cell is shown and outlined. (a)–(d) Oscillations of the electron density and the electron-current density with frequency ω at phases ωt equal to (a) 0; (b) $\pi/2$; (c) π and (d) $3\pi/2$. (e)–(h) Oscillations of the electron density and the electron-current density with frequency 2ω at phases $2\omega t$ equal to (e) 0; (f) $\pi/2$; (g) π and (h) $3\pi/2$. (i)–(l) Oscillations of the electron density and the electron-current density with frequency 3ω at phases $3\omega t$ equal to (i) 0; (j) $\pi/2$, (k) π and (l) $3\pi/2$. electron-current density above a threshold of 3 a.u., 0.003 a.u. and 0.002 a.u. for the first, second and third orders, respectively, is shown and lengths of the vectors are scaled logarithmically. XOWM signal at $\mathbf{G} = (1,2,0)$ with highlighted side peaks that correspond to a certain order of optical response are shown in the same raws with the oscillations of this order, namely, (m) the side peaks shifted by $\pm\omega$, (n) the side peaks shifted by $\pm 2\omega$ and (o) the side peaks shifted by $\pm 3\omega$ relative to ω_{in} are highlighted.

time-unresolved experiment as an example. Here, we use this framework to develop a method to reveal insights into laser-driven electron dynamics by means of ultrafast x-ray scattering from a laser-driven material.

The total Hamiltonian of a crystal, an optical field and a probe x-ray pulse is given by

$$\hat{H} = \hat{H}_{\text{el}} + \hat{H}_{\text{into}} + \hat{H}_{\text{intx}} + \hat{H}_{\text{o}} + \hat{H}_{\text{x}}, \tag{1}$$

where $\hat{H}_{\text{el}}$ is the Hamiltonian of the crystal, $\hat{H}_{\text{into}}$ and $\hat{H}_{\text{intx}}$ are the Hamiltonians that describe the interaction of the crystal with the optical driving field and with the x-ray pulse, respectively. $\hat{H}_{\text{o}}$ and $\hat{H}_{\text{x}}$ are Hamiltonians of the optical and the x-ray fields, respectively. The interaction Hamiltonian $\hat{H}_{\text{into}}$ is given by $\frac{1}{c}\int d^3r \hat{\psi}^\dagger(\mathbf{r})(\hat{\mathbf{A}}_{\text{o}} \cdot \hat{\mathbf{p}})\hat{\psi}(\mathbf{r})$, where $\hat{\psi}$ ($\hat{\psi}^\dagger$) are electron annihilation (creation) field operators, $\hat{\mathbf{A}}_{\text{o}}$ is the vector potential of the optical field, $\hat{\mathbf{p}}$ is the momentum operator, c is the speed of light. This

and the following expressions are in atomic units. We neglect the term proportional to $\hat{\mathbf{A}}_{\mathrm{o}}^2$ in the interaction between the electronic system and the optical field. We describe the interaction with the optical field within the dipole approximation.

We assume that the photon energy of the x-ray pulse is in the hard x-ray region and is nonresonant with any core-excitation energy of the crystal. In this case, resonant x-ray scattering governed by the term proportional to $\hat{\mathbf{A}}_{\mathrm{x}} \cdot \hat{\mathbf{p}}$ becomes negligible and the interaction of the electronic system and the x-ray pulse is given by the Hamiltonian $\hat{H}_{\mathrm{intx}} = 1/(2c^2) \int d^3r \hat{\psi}^\dagger(\mathbf{r}) \hat{\mathbf{A}}_{\mathrm{x}}^2 \hat{\psi}(\mathbf{r})$ that describes nonresonant x-ray scattering. Elastic nonresonant x-ray scattering forms the basis for x-ray diffraction techniques, since it connects the scattering signal to the Fourier transform of the electron density [49–51]. The $\hat{\mathbf{A}}_{\mathrm{x}}^2$-interaction term can also lead to inelastic scattering.

In the presence of the optical field, both elastic and inelastic x-ray scattering signals get modulated and the total x-ray scattering probability is given by $P_{\mathrm{tot.}} = P_{\mathrm{q.e.}} + P_{\mathrm{inel.}}$. We refer to the scattering signal that results due to the optically-induced modulation of elastic scattering, as quasielastic scattering and its probability as $P_{\mathrm{q.e.}}$. As we will show, it contains the relevant information about the optically-driven dynamics in a material. It is still necessary to compute the probability of inelastic scattering, $P_{\mathrm{inel.}}$, to ensure that it does not suppress the quasielastic scattering signal. For α-quartz, we find that it is two orders of magnitude smaller than the quasielastic scattering signal in the spectral range that we will consider.

Let us briefly review the case when the duration of the x-ray probe pulse is longer than one cycle of the optical driving field. The resulting x-ray scattering signal can be understood by analogy to conventional x-ray-diffraction signals. An x-ray-diffraction signal from a crystal consists of Bragg peaks resulting from elastic scattering. The intensity of the Bragg peak at reciprocal-lattice vector $\mathbf{G}$ is proportional to the corresponding Fourier component of the electron density of the crystal squared, $|\int d^3r e^{i\mathbf{G}\cdot\mathbf{r}} \rho(\mathbf{r})|^2$. When x-ray and optical fields simultaneously interact with a crystal, wave mixing occurs, leading to sum and difference frequency generation [36, 37]. Sum and difference frequency generation manifest themselves as side peaks to Bragg peaks that are energetically separated from them by multiples of the optical driving frequency, $\mu\omega$. The intensity of the side peaks of the Bragg peak at $\mathbf{G}$ of order μ is given by the Fourier transform $|\int d^3r e^{i\mathbf{G}\cdot\mathbf{r}} \widetilde{\rho}_\mu(\mathbf{r})|^2$, where $\widetilde{\rho}_\mu(\mathbf{r})$ is the associated Fourier amplitude of the time-dependent electron density oscillating in a periodic optical field [48]

$$\rho(\mathbf{r}, t) = \sum_\mu \widetilde{\rho}_\mu(\mathbf{r}) e^{i\mu\omega t}. \tag{2}$$

Figures 1 (m)-(o) show the calculated x-ray-optical wave mixing signal for the Bragg peak at $\mathbf{G} = (1, 2, 0)$ and its side peaks up to the third order. Here, $\mathbf{G}$ is represented in terms of integer multiples of the primitive reciprocal lattice vectors and is parallel to $(\sqrt{3}, \sqrt{2}, 0)$. Different subfigures show the same signal, in which μth-order side peaks that are related to the Fourier transform of the density oscillations shown in the same row in Fig. 1 are highlighted.

Generally, the probability of quasielastic x-ray scattering of a Gaussian-shaped x-ray pulse with duration τ_p is given by [48]

$$P_{\mathrm{q.e.}}(\omega_\mathrm{s},\mathbf{G}) = P_0 \sum_\mu \mathcal{E}_\mu^2 \left| \int d^3r e^{i\mathbf{G}\cdot\mathbf{r}} \widetilde{\rho}_\mu(\mathbf{r}) \right|^2 \tag{3}$$
$$+ (-1)^{\Delta\mu} P_0 \sum_{\mu,\Delta\mu>0} 2\,\mathrm{Re}\left[\mathcal{E}_\mu \mathcal{E}_{\mu+\Delta\mu} e^{i\Delta\mu\omega t_p} \int d^3r e^{i\mathbf{G}\cdot\mathbf{r}} \widetilde{\rho}_\mu(\mathbf{r}) \int d^3r e^{-i\mathbf{G}\cdot\mathbf{r}} \widetilde{\rho}^*_{\mu+\Delta\mu}(\mathbf{r}) \right].$$

Here, $P_0 = \sum_{s_\mathrm{s}} |(\boldsymbol{\epsilon}_\mathrm{in}\cdot\boldsymbol{\epsilon}^*_{x,\boldsymbol{\kappa}_\mathrm{s},s_\mathrm{s}})|^2 \omega_\mathrm{s}^2/(4\pi^2\omega_\mathrm{in}^2 c^3)$, where $\boldsymbol{\epsilon}_\mathrm{in}$ is the mean polarization vector of the incoming x-ray beam, ω_s is the energy of a scattered photon with momentum $\boldsymbol{\kappa}_\mathrm{s}$, the sum over s_s refers to the sum over polarization vectors of the scattered photons $\boldsymbol{\epsilon}^*_{x,\boldsymbol{\kappa}_\mathrm{s}s_\mathrm{s}}$ and ω_in is the mean photon energy of the incoming x-ray beam. t_p is the time of x-ray-pulse arrival relative to a reference time $t = 0$, when the phase ωt_p and the optical electric field are zero. $\mathcal{E}_\mu = \sqrt{\frac{\tau_p^2\pi}{2\ln 2}} e^{-(\omega_\mathrm{s}-\omega_\mathrm{in}-\mu\omega)^2\tau_p^2/8\ln 2}$ are Gaussian-shaped functions centered at the positions of the side peaks. Their width is inversely proportional to the x-ray-probe pulse duration. A product of such two Gaussians is also a Gaussian function centered in the middle between their centers.

If the duration of the probe pulse is longer than one cycle of the optical driving field, the Gaussian-shaped functions are spectrally narrow and peaks centered at different positions do not spectrally overlap. Any product $\mathcal{E}_\mu\mathcal{E}_{\mu+\Delta\mu}$ for $\Delta\mu \neq 0$ is negligible and the second term in Eq. (3) vanishes. A quasielastic scattering signal then consists of isolated peaks with a time-independent intensity as shown in Figs. 1 (m)-(o).

When the duration of the probe pulse decreases, the spectral peaks get broader and start interfering. The second term in Eq. (3) becomes nonzero and the intensity of the signal becomes time-dependent. We adjust the x-ray-pulse duration such that only nearest-neighbour side peaks can spectrally overlap. This is achieved for an x-ray pulse duration of 2.35 fs for the case of an optical field with a photon energy of 1.2 eV, corresponding to an optical period of 3.4 fs. In this case, the interference terms are proportional to Gaussian functions centered in the middle between nearest-neighbour side peaks, *i.e.* at $\omega_\mathrm{s} = \omega_\mathrm{in} + (\mu + 1/2)\omega$.

Figure 2 shows the sub-cycle-resolved x-ray-optical wave mixing signal by a probe x-ray pulse with duration of 2.35 fs at $\mathbf{G} = (1,1,2)$ and $\mathbf{G} = (-1,-1,-2)$. The signal evolves in time with the period $T = 2\pi/\omega$ in agreement with Eq. (3). We observe that the signal is no longer centrosymmetric in momentum space in contrast to the time-independent case. The quasielastic scattering signal is also not symmetric with respect to the scattered energy.

Let us analyze the time and momentum dependences of the signal to releave the origin of centrosymmetry breaking. The momentum dependence of the signal is due to the Fourier components of the amplitudes of the electron density. The Fourier components of the density amplitudes can be represented as a sum of a centrosymmetric and an antisymmetric function $\int d^3r e^{i\mathbf{G}\cdot\mathbf{r}}\widetilde{\rho}_\mu(\mathbf{r}) = \int d^3r \cos(\mathbf{G}\cdot\mathbf{r})\widetilde{\rho}_\mu(\mathbf{r}) + i\int d^3r \sin(\mathbf{G}\cdot\mathbf{r})\widetilde{\rho}_\mu(\mathbf{r})$. In materials with time reversal symmetry, which includes α-quartz, the even-order density amplitudes $\widetilde{\rho}_{\mu_\mathrm{even}}(\mathbf{r})$ are real functions and the odd-order density amplitudes $\widetilde{\rho}_{\mu_\mathrm{odd}}(\mathbf{r})$ are purely imaginary, *i.e.* they have a phase that is either $n\pi$ or $(n+1)\pi/2$,

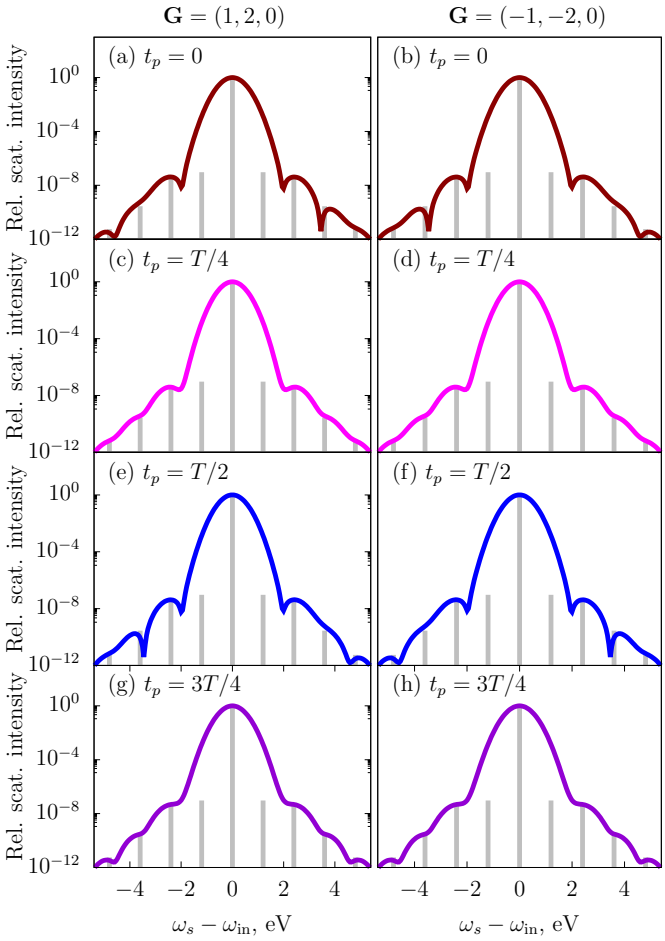

Fig. 2 X-ray scattering signal at $\mathbf{G} = (1, 2, 0)$ and $\mathbf{G} = (-1, -2, 0)$ from the laser-dressed α-quartz crystal at different probe-pulse arrival times as a function of $\omega_{\text{s}} - \omega_{\text{in}}$. The signal at (a) $\mathbf{G} = (1, 2, 0)$ and (b) $\mathbf{G} = (-1, -2, 0)$ is shown for the probe-pulse arrival time $t_p = 0$; at (c) $\mathbf{G} = (1, 2, 0)$ and (d) $\mathbf{G} = (-1, -2, 0)$ is shown for $t_p = T/4$; at (e) $\mathbf{G} = (1, 2, 0)$ and (f) $\mathbf{G} = (-1, -2, 0)$ is shown for $t_p = T/2$ and at (g) $\mathbf{G} = (1, 2, 0)$ and (h) $\mathbf{G} = (-1, -2, 0)$ is shown for $t_p = 3T/4$. The signal is normalized to the intensity of the main Bragg peak of α-quartz at $\mathbf{G} = (1, 2, 0)$. The gray vertical lines are situated at the positions of the side peaks, $\omega_{\text{s}} - \omega_{\text{in}} - \mu\omega$, and their heights correspond to the relative intensities of the side peaks in the absence of interference.

where n is an integer [35]. The phases of the $\widetilde{\rho}_{\mu}(\mathbf{r})$ determine the phases of the symmetric and antisymmetric parts of the Fourier components. We employ these dependencies

to express the antisymmetric part of the signal as

$$
\begin{aligned}
&[P_{\mathrm{q.e.}}(\omega_{\mathrm{s}},\mathbf{G}) - P_{\mathrm{q.e.}}(\omega_{\mathrm{s}},-\mathbf{G})]/2 = \\
&= P_0\cos(\omega t_p)\sum_{\mu} 2\mathcal{E}_{\mu}\mathcal{E}_{\mu+1}\left[i\int d^3r\,\sin(\mathbf{G}\cdot\mathbf{r})\widetilde{\rho}_{\mu}(\mathbf{r})\int d^3r\,\cos(\mathbf{G}\cdot\mathbf{r})\widetilde{\rho}_{\mu+1}(\mathbf{r})\right. \\
&\qquad\left. -i\int d^3r\,\cos(\mathbf{G}\cdot\mathbf{r})\widetilde{\rho}_{\mu}(\mathbf{r})\int d^3r\,\sin(\mathbf{G}\cdot\mathbf{r})\widetilde{\rho}_{\mu+1}(\mathbf{r})\right].
\end{aligned}
\tag{4}
$$

We find that it evolves in time as $\cos(\omega t_p)$. At the same time, the phases of the density amplitudes also determine the oscillation phases of the electron density that evolves as

$$
\rho(\mathbf{r},t) = \widetilde{\rho}_0(\mathbf{r}) - \varrho_1(\mathbf{r})\sin(\omega t) + \varrho_2(\mathbf{r})\cos(2\omega t) - \varrho_3(\mathbf{r})\sin(3\omega t) + \cdots, \tag{5}
$$

and, via the continuity equation, those of the electron-current density,

$$
\mathbf{j}(\mathbf{r},t) = -\mathbf{j}_1(\mathbf{r})\cos(\omega t) - \mathbf{j}_2(\mathbf{r})\sin(2\omega t) - \mathbf{j}_3(\mathbf{r})\cos(3\omega t) - \cdots \tag{6}
$$

Here, $\varrho_{\mu_{\mathrm{even}}}(\mathbf{r}) = 2\,\mathrm{Re}[\widetilde{\rho}_{\mu_{\mathrm{even}}}(\mathbf{r})]$, $\varrho_{\mu_{\mathrm{odd}}}(\mathbf{r}) = 2\,\mathrm{Im}[\widetilde{\rho}_{\mu_{\mathrm{odd}}}(\mathbf{r})]$ and $\mathbf{j}_{\mu}$ are real-valued amplitudes of the electron density and electron-current density, respectively. Thus, we find that the antisymmetric part of the sub-cycle-resolved x-ray-optical wave mixing signal evolves in time as the first-order oscillation of the electron-current density and is maximal at $t_p = 0$ and $t_p = T/2$. At these two times during the period, the first-order oscillation of the electron-current density has a maximal magnitude and the first-order oscillation of the electron density is zero (see Fig. 1(a)–(c)). The quasielastic scattering signal is centrosymmetric in momentum space at times $t_p = T/4$ and $t_p = 3T/4$, when the first-order electron-current density vanishes.

The signal in Fig. 2 is sensitive only to the first-order oscillation of microscopic optical response, since we selected a probe-pulse duration that is longer than the period of the second-order oscillation with the frequency 2ω. If the probe-pulse duration is chosen short enough to resolve an nth-order oscillation with the frequency $n\omega$, the signal would have oscillating terms with frequencies ω, 2ω, $\cdots$, $n\omega$. The oscillation with the frequency $\Delta\mu\omega$ would be due to interference terms between μ and $\mu + \Delta\mu$ side peaks. Even in this case, the connection of the antisymmetric part of the signal to oscillations of the electron-current density still holds. The antisymmetric part of the signal would consist of time-dependent terms that oscillate either as $\cos(\Delta\mu\omega t_p)$ for odd $\Delta\mu$ or as $\sin(\Delta\mu\omega t_p)$ for even $\Delta\mu$. Thus, the time evolution of the antisymmetric part of the signal correlates with the time evolution of the electron-current density in Eq. (6). A similar effect of momentum-symmetry breaking of time- and momentum-resolved x-ray signals from a nonstationary electron system that correlates in time with currents has been predicted for other types of pump-probe experiments as well [52–55].

Analyzing the centrosymmetric part of the signal, $[P_{\mathrm{q.e.}}(\omega_{\mathrm{s}},\mathbf{G}) + P_{\mathrm{q.e.}}(\omega_{\mathrm{s}},-\mathbf{G})]/2$, we find that it oscillates as $\sin(\omega t_p)$, which is in phase with the first-order oscillation of the electron density. This connection can also be generalized for high-order oscillations of the signal, if the temporal resolution is sufficient to resolve them. The

centrosymmetric part of the signal would consist of a time-independent part and a time-dependent part due to interference terms between μ and $\mu+\Delta\mu$ side peaks. They would oscillate as $\sin(\Delta\mu\omega t_p)$ for odd $\Delta\mu$ or as $\cos(\Delta\mu\omega t_p)$ for even $\Delta\mu$, which correlates with oscillations of the electron density. Thus, we find that the phases of temporal oscillations of the density and those of the electron-current density are encoded in the temporal behavior of the centrosymmetric and antisymmetric parts, respectively.

Let us analyze the signal in Fig. 2 from a different perspective. We now focus only on the time dependence of the quasielastic scattering signal and find that it can be represented as

$$P_{\text{q.e.}}(\omega_{\text{s}},\mathbf{G}) = \frac{P_0}{4}\sum_{\mu}\mathcal{E}_{\mu}^2|\mathcal{P}_{\mu}(\mathbf{G})|^2 \tag{7}$$
$$+\frac{P_0}{2}\sum_{\mu}(-1)^{\mu+1}\mathcal{E}_{\mu}\mathcal{E}_{\mu+1}|\mathcal{P}_{\mu}(\mathbf{G})||\mathcal{P}_{\mu+1}(\mathbf{G})|\sin(\omega t_p+\alpha_{\mu}(\mathbf{G})-\alpha_{\mu+1}(\mathbf{G})),$$

where we expressed the Fourier transform of the real-valued amplitudes of the electron density as $\int d^3r e^{i\mathbf{G}\cdot\mathbf{r}}\varrho_{\mu}(\mathbf{r}) = \mathcal{P}_{\mu}(\mathbf{G}) = |\mathcal{P}_{\mu}(\mathbf{G})|\, e^{i\alpha_{\mu}(\mathbf{G})}$. The optical electric field oscillates as $\sin(\omega t)$ and the time-evolution of the sub-cycle-resolved x-ray-optical wave mixing signal comprises oscillations that display a phase shift with respect to the electric-field oscillation. The phase difference in time is determined by the momentum-dependent phases of the Fourier components of the optically-induced charge distributions, $\alpha_{\mu}(\mathbf{G})$.

The quasielastic signal provides both the phases $\alpha_{\mu}(\mathbf{G})$ and the amplitudes $|\mathcal{P}_{\mu}(\mathbf{G})|$ of the Fourier components of the optically-induced charge distributions $\varrho_{\mu}(\mathbf{r})$ of all orders μ as we will show with the expression in Eq. (7). This is a big advantage of a time-resolved measurement over a time-unresolved one. Knowledge of the amplitudes and phases of the Fourier components of a density at all $\mathbf{G}$ provides the complete information to reconstruct it. Especially, the phases are crucial for the reconstruction; the "phase problem", i.e., the lack of phase information, is a well-known problem in crystallography [56]. A time-unresolved measurement that leads to separated side peaks (see Figs. 1 (m)-(o)) provides only the amplitudes $|\mathcal{P}_{\mu}(\mathbf{G})|$ of the Fourier components. A time-resolved measurement provides also the phases as we show below.

For the phase retrieval, we need to know the phase of the Fourier component of the unperturbed density $\alpha_0(\mathbf{G})$, which is not a problem for an experiment performed on a material with a known structure. Figure 3 shows the time-dependent part of the signal at different t_p in the spectral range centered around $\omega_{\text{in}}+\omega/2$. From Eq. (7), we know that it is given by the interference term between the main peak and the first-order side peak, which oscillates as $-\sin(\omega t_p+\alpha_0-\alpha_1)$. Here, we subtracted the time-independent part of the signal from the total signal. The time-independent part is given by the centrosymmetric part of the signal at time $t_p=0$, $[P_{\text{q.e.}}(\mathbf{G},t_p=0)+P_{\text{q.e.}}(-\mathbf{G},t_p=0)]/2$. The time-dependent signal in Fig. 3 oscillates as $-\sin(0.012\pi+\omega t_p)$ and we determine that $\alpha_1(\mathbf{G})=\alpha_0(\mathbf{G})-0.012\pi$. The interference term between the first-order and the second-order side peak is centered at $\omega_{\text{in}}+3\omega/2$ and oscillates as $\sin(\omega t_p+\alpha_1-\alpha_2)$ and this is how we can find $\alpha_2(\mathbf{G})$. This procedure can then be repeated for the subsequent orders.

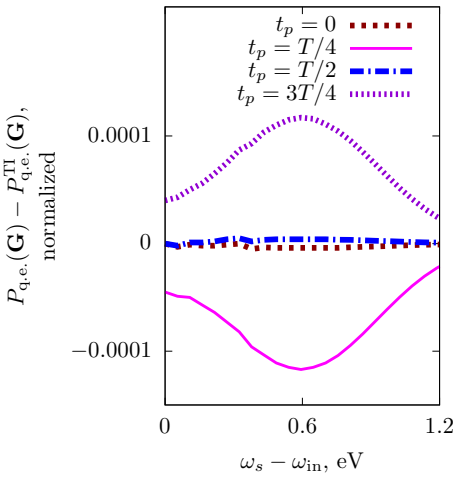

Fig. 3 Time-dependent part of the x-ray scattering signal at $\mathbf{G} = (1, 2, 0)$ at different probe-pulse arrival times as a function of $\omega_{\rm s} - \omega_{\rm in}$. The signal is normalized to the intensity of the main Bragg peak of α-quartz at $\mathbf{G} = (1, 2, 0)$.

The amplitudes $|\mathcal{P}_\mu(\mathbf{G})|$ of the Fourier components can be reconstructed either from a time-independent measurement or from the time-independent part of the signal that is given by Gaussians centered at $\mu\omega_{\rm in}$ with the intensity proportional to $|\mathcal{P}_\mu(\mathbf{G})|^2$. This way, we obtain the Fourier components $\mathcal{P}_\mu(\mathbf{G})$ including the amplitude and the phase. Measuring the sub-cycle-resolved x-ray-optical wave mixing signal at various $\mathbf{G}$, one can reconstruct charge distributions $\varrho_\mu(\mathbf{r})$ for all orders of microscopic optical response μ. In a real experiment, orders with small amplitudes like the third and the fourth ones in our case would be very challenging to detect and reconstruct, but there are no fundamental restrictions to reconstruct them.

The directions of electron currents can also be retrieved once the charge distributions have been reconstructed. The amplitudes of the electron density and the electron current densities are connected via the continuity equation as $\mathrm{div}\,\mathbf{j}_\mu(\mathbf{r}) = -\mu\omega\varrho_\mu(\mathbf{r})$. Their Fourier transforms are connected via

$$\int d^3r e^{i\mathbf{G}\cdot\mathbf{r}}\varrho_\mu(\mathbf{r}) = \frac{i}{\mu\omega}\mathbf{G}\cdot\int d^3r e^{i\mathbf{G}\cdot\mathbf{r}}\mathbf{j}_\mu(\mathbf{r}) \tag{8}$$

due to the Green's first identity, if the surface integral of the electron current density vanishes. For example, the first-order electron-current density is unidirectional and parallel to the light polarization axis $\boldsymbol{\epsilon}_o$. The intensity of the first-order side peak is given by $|\int d^3r e^{i\mathbf{G}\cdot\mathbf{r}}\varrho_1(\mathbf{r})|^2$ and must then scale as $|(\boldsymbol{\epsilon}_o\cdot\mathbf{G})|^2$, which agrees with the experimental observation in Ref. [38]. With our method, we can reconstruct the projection of the Fourier components of the electron-current density including phases. The sign of the projections reveals the direction of the current and the phases reveal spatial symmetry features of the electron-current density.

Conclusion

When light interacts with a material, charges rearrange within its unit cell forming complex structures. Microscopic electron currents that can point in different directions are induced. Such microscopic optical response can be detected with x rays due to their short wavelength. Here, we proposed a method to reconstruct oscillations of charge and electron-current density distributions employing ultrafast x-ray diffraction during the time a material is driven by light, namely, by sub-cycle-resolved x-ray-optical wave mixing.

The sub-cycle-resolved x-ray-optical wave mixing signal $P_{\mathrm{q.e.}}(\mathbf{G}, t_p)$ is notably noncentrosymmetric with respect to the scattering vector $\mathbf{G}$. The temporal evolution of the antisymmetric part of the signal, $(P_{\mathrm{q.e.}}(\mathbf{G}, t_p) - P_{\mathrm{q.e.}}(-\mathbf{G}, t_p))/2$ reveals the phases of the temporal oscillations of the electron-current density. The temporal evolution of the centrosymmetric part of the signal, $(P_{\mathrm{q.e.}}(\mathbf{G}, t_p) + P_{\mathrm{q.e.}}(-\mathbf{G}, t_p))/2$ reveals the phases of thetemporal oscillations of the electron density. Furthermore, the signal encodes the $\mathbf{G}$th Fourier components of charge distributions and projections of the $\mathbf{G}$th Fourier components of electron-current density distributions. The amplitudes of the Fourier components can be reconstructed from the time-independent part of the signal. The phases of the Fourier components can be reconstructed from the phases of the temporal oscillations of the time-dependent part of the signal. If both phases and amplitudes of the Fourier components at various $\mathbf{G}$ can be measured, then the optically-induced charge distributions can be completely reconstructed. An atomically-resolved view into light-matter interactions will provide a deeper understanding of optically-driven electron dynamics and prompt further developments of nonlinear optics towards technological applications.

Methods

Kohn-Sham wave functions were calculated using the ABINIT software package [57–60] with Perdew-Burke-Ernzerhof functionals [61, 62]. We took into account 24 valence and 216 conduction bands on a $16 \times 16 \times 16$ $\mathbf{k}$-point grid. The calculated Kohn-Sham wave functions were used to construct the Floquet-Bloch Hamiltonian as described in Refs. [35, 48]. The infinite Floquet-Bloch Hamiltonian was approximated by a matrix with 141 blocks, each containing 240 states. The number of $\mathbf{k}$-points, conduction bands and blocks were increased until convergence was reached. We applied the scissors approximation [63] to correct the band gap from the calculated 6.1 eV to the experimental value of 8.9 eV [64]. Optically-induced charge oscillations and electron current densities were calculated as described in Ref. [35] and visualized using VESTA [65]. α-quartz is chiral and has two structural types; we considered the type with space group 152.

Data availability

The data that support the findings of this study are available from the corresponding author upon reasonable request.

Code availability

The code used to produce the results of this study is available from the corresponding author upon reasonable request.

References

[1] Schiffrin, A. *et al.* Optical field-induced current in dielectrics. *Nature* **493**, 70–74 (2012). URL http://dx.doi.org/10.1038/nature11567.

[2] Schultze, M. *et al.* Controlling dielectrics with the electric field of light. *Nature* **493**, 75–78 (2012). URL http://dx.doi.org/10.1038/nature11720.

[3] Chai, X. *et al.* Subcycle terahertz nonlinear optics. *Phys. Rev. Lett.* **121**, 143901 (2018). URL https://link.aps.org/doi/10.1103/PhysRevLett.121.143901.

[4] Sederberg, S. *et al.* Vectorized optoelectronic control and metrology in a semiconductor. *Nature Photonics* (2020). URL https://doi.org/10.1038/s41566-020-0690-1.

[5] Kuehn, W. *et al.* Coherent ballistic motion of electrons in a periodic potential. *Phys. Rev. Lett.* **104**, 146602 (2010). URL http://link.aps.org/doi/10.1103/PhysRevLett.104.146602.

[6] Schubert, O. *et al.* Sub-cycle control of terahertz high-harmonic generation by dynamical bloch oscillations. *Nature Photonics* **8**, 119–123 (2014). URL http://dx.doi.org/10.1038/nphoton.2013.349.

[7] Sommer, A. *et al.* Attosecond nonlinear polarization and light–matter energy transfer in solids. *Nature* **534**, 86–90 (2016). URL https://doi.org/10.1038/nature17650.

[8] Schlaepfer, F. *et al.* Attosecond optical-field-enhanced carrier injection into the gaas conduction band. *Nature Physics* **14**, 560–564 (2018). URL https://doi.org/10.1038/s41567-018-0069-0.

[9] Hübener, H., Sentef, M. A., De Giovannini, U., Kemper, A. F. & Rubio, A. Creating stable floquet-weyl semimetals by laser-driving of 3d dirac materials. *Nature Communications* **8**, 13940 (2017).

[10] Oka, T. & Kitamura, S. Floquet engineering of quantum materials. *Annual Review of Condensed Matter Physics* **10**, 387–408 (2019). URL https://doi.org/10.1146/annurev-conmatphys-031218-013423.

[11] Nuske, M. *et al.* Floquet dynamics in light-driven solids. *Phys. Rev. Research* **2**, 043408 (2020). URL https://link.aps.org/doi/10.1103/PhysRevResearch.2.043408.

[12] Uzan, A. J. *et al.* Attosecond spectral singularities in solid-state high-harmonic generation. *Nature Photonics* **14**, 183–187 (2020). URL https://doi.org/10.1038/s41566-019-0574-4.

[13] Ghimire, S. *et al.* Observation of high-order harmonic generation in a bulk crystal. *Nature Physics* **7**, 138–141 (2010). URL http://dx.doi.org/10.1038/nphys1847.

[14] Goulielmakis, E. & Brabec, T. High harmonic generation in condensed matter. *Nature Photonics* **16**, 411–421 (2022). URL https://doi.org/10.1038/s41566-022-00988-y.

[15] Schoetz, J. *et al.* Perspective on petahertz electronics and attosecond nanoscopy. *ACS Photonics* **6**, 3057–3069 (2019). URL https://doi.org/10.1021/acsphotonics.9b01188.

[16] Ossiander, M. *et al.* The speed limit of optoelectronics. *Nature Communications* **13**, 1620 (2022). URL https://doi.org/10.1038/s41467-022-29252-1.

[17] Mashiko, H., Oguri, K., Yamaguchi, T., Suda, A. & Gotoh, H. Petahertz optical drive with wide-bandgap semiconductor. *Nature Physics* **12**, 741–745 (2016). URL https://doi.org/10.1038/nphys3711.

[18] Zimin, D. A. *et al.* Dynamic optical response of solids following 1-fs-scale photoinjection. *Nature* **618**, 276–280 (2023). URL https://doi.org/10.1038/s41586-023-05986-w.

[19] Kruchinin, S. Y., Krausz, F. & Yakovlev, V. S. Colloquium: Strong-field phenomena in periodic systems. *Rev. Mod. Phys.* **90**, 021002 (2018). URL https://link.aps.org/doi/10.1103/RevModPhys.90.021002.

[20] Inzani, G. *et al.* Field-driven attosecond charge dynamics in germanium. *Nature Photonics* **17**, 1059–1065 (2023). URL https://doi.org/10.1038/s41566-023-01274-1.

[21] You, Y. S., Reis, D. A. & Ghimire, S. Anisotropic high-harmonic generation in bulk crystals. *Nature Physics* **13**, 345 (2016). URL http://www.nature.com/nphys/journal/vaop/ncurrent/full/nphys3955.html.

[22] Ndabashimiye, G. *et al.* Solid-state harmonics beyond the atomic limit. *Nature* **534**, 520–523 (2016).

[23] Lakhotia, H. *et al.* Laser picoscopy of valence electrons in solids. *Nature* **583**, 55–59 (2020). URL https://doi.org/10.1038/s41586-020-2429-z.

[24] Mitrano, M. & Wang, Y. Probing light-driven quantum materials with ultrafast resonant inelastic x-ray scattering. *Communications Physics* **3**, 184 (2020). URL https://doi.org/10.1038/s42005-020-00447-6.

[25] Teichmann, S. M., Silva, F., Cousin, S. L., Hemmer, M. & Biegert, J. 0.5-kev soft x-ray attosecond continua. *Nature Communications* **7**, 11493 (2016). URL https://doi.org/10.1038/ncomms11493.

[26] Huang, S. *et al.* Generating single-spike hard x-ray pulses with nonlinear bunch compression in free-electron lasers. *Phys. Rev. Lett.* **119**, 154801 (2017). URL https://link.aps.org/doi/10.1103/PhysRevLett.119.154801.

[27] Parc, Y. W., Shim, C. H. & Kim, D. E. Toward the generation of an isolated tw-attosecond x-ray pulse in xfel. *Applied Sciences* **8** (2018). URL https://www.mdpi.com/2076-3417/8/9/1588.

[28] Li, J. *et al.* 53-attosecond x-ray pulses reach the carbon k-edge. *Nature communications* **8**, 186 (2017).

[29] Kaertner, F. *et al.* AXSIS: Exploring the frontiers in attosecond X-ray science, imaging and spectroscopy. *Nuclear Instruments and Methods in Physics Research Section A: Accelerators, Spectrometers, Detectors and Associated Equipment* **829**, 24 – 29 (2016). URL http://www.sciencedirect.com/science/article/pii/S0168900216002564.

[30] Duris, J. *et al.* Tunable isolated attosecond x-ray pulses with gigawatt peak power from a free-electron laser. *Nature Photonics* **14**, 30–36 (2020). URL https://doi.org/10.1038/s41566-019-0549-5.

[31] Sidiropoulos, T. P. H. *et al.* Probing the energy conversion pathways between light, carriers, and lattice in real time with attosecond core-level spectroscopy. *Phys. Rev. X* **11**, 041060 (2021). URL https://link.aps.org/doi/10.1103/PhysRevX.11.041060.

[32] Sidiropoulos, T. P. H. *et al.* Enhanced optical conductivity and many-body effects in strongly-driven photo-excited semi-metallic graphite. *Nature Communications* **14**, 7407 (2023). URL https://doi.org/10.1038/s41467-023-43191-5.

[33] Siegrist, F. *et al.* Light-wave dynamic control of magnetism. *Nature* **571**, 240–244 (2019). URL https://doi.org/10.1038/s41586-019-1333-x.

[34] Jin, W. *et al.* Observation of a ferro-rotational order coupled with second-order nonlinear optical fields. *Nature Physics* **16**, 42–46 (2020). URL https://doi.org/10.1038/s41567-019-0695-1.

[35] Popova-Gorelova, D. & Santra, R. Microscopic nonlinear optical response: Analysis and calculations with the Floquet–Bloch formalism. *Structural Dynamics* **11**, 014102 (2024). URL https://doi.org/10.1063/4.0000220.

[36] Freund, I. & Levine, B. F. Optically modulated x-ray diffraction. *Phys. Rev. Lett.* **25**, 1241–1245 (1970). URL https://link.aps.org/doi/10.1103/PhysRevLett.

25.1241.

[37] Eisenberger, P. M. & McCall, S. L. Mixing of x-ray and optical photons. *Phys. Rev. A* **3**, 1145–1151 (1971). URL https://link.aps.org/doi/10.1103/PhysRevA.3.1145.

[38] Glover, T. E. *et al.* X-ray and optical wave mixing. *Nature* **488**, 603–608 (2012). URL http://www.nature.com/nature/journal/v488/n7413/full/nature11340.html.

[39] Boemer, C. *et al.* Towards novel probes for valence charges via x-ray optical wave mixing. *Faraday Discuss.* – (2021). URL http://dx.doi.org/10.1039/D0FD00130A.

[40] Ornelas-Skarin, C. *et al.* Nonlinear x-ray optical wave-mixing in silicon. *Optica Nonlinear Optics Topical Meeting 2023* **Th2**, Th2A.3 (2023). URL https://opg.optica.org/abstract.cfm?URI=NLO-2023-Th2A.3.

[41] Yu, C. *et al.* Dependence of high-order-harmonic generation on dipole moment in Sio_2 crystals. *Phys. Rev. A* **94**, 013846 (2016). URL https://link.aps.org/doi/10.1103/PhysRevA.94.013846.

[42] Luu, T. T. & Wörner, H. J. Observing broken inversion symmetry in solids using two-color high-order harmonic spectroscopy. *Phys. Rev. A* **98**, 041802 (2018). URL https://link.aps.org/doi/10.1103/PhysRevA.98.041802.

[43] Otobe, T. High-harmonic generation in α-quartz by electron-hole recombination. *Phys. Rev. B* **94**, 235152 (2016). URL https://link.aps.org/doi/10.1103/PhysRevB.94.235152.

[44] Luu, T. T., Scagnoli, V., Saha, S., Heyderman, L. J. & Wörner, H. J. Generation of coherent extreme ultraviolet radiation from α–quartz using 50??fs laser pulses at a 1030??nm wavelength and high repetition rates. *Opt. Lett.* **43**, 1790–1793 (2018). URL https://opg.optica.org/ol/abstract.cfm?URI=ol-43-8-1790.

[45] Heinrich, T. *et al.* Chiral high-harmonic generation and spectroscopy on solid surfaces using polarization-tailored strong fields. *Nature Communications* **12**, 3723 (2021). URL https://doi.org/10.1038/s41467-021-23999-9.

[46] Shao, M., Liang, F., Zhang, Z., Yu, H. & Zhang, H. Spatial frequency manipulation of a quartz crystal for phase-matched second-harmonic vacuum ultraviolet generation. *Laser & Photonics Reviews* **17**, 2300244 (2023). URL https://onlinelibrary.wiley.com/doi/abs/10.1002/lpor.202300244.

[47] Garg, M., Kim, H. Y. & Goulielmakis, E. Ultimate waveform reproducibility of extreme-ultraviolet pulses by high-harmonic generation in quartz. *Nature Photonics* **12**, 291–296 (2018). URL https://doi.org/10.1038/s41566-018-0123-6.

[48] Popova-Gorelova, D., Reis, D. A. & Santra, R. Theory of x-ray scattering from laser-driven electronic systems. *Phys. Rev. B* **98**, 224302 (2018). URL https://link.aps.org/doi/10.1103/PhysRevB.98.224302.

[49] Eisenberger, P. & Platzman, P. M. Compton scattering of x rays from bound electrons. *Phys. Rev. A* **2**, 415–423 (1970). URL https://link.aps.org/doi/10.1103/PhysRevA.2.415.

[50] Hau-Riege, S. *Nonrelativistic Quantum X-Ray Physics* (Wiley, 2015). URL https://books.google.de/books?id=qzXOBgAAQBAJ.

[51] Santra, R. Concepts in x-ray physics. *Journal of Physics B: Atomic, Molecular and Optical Physics* **42**, 023001 (2008). URL https://dx.doi.org/10.1088/0953-4075/42/2/023001.

[52] Dixit, G., Vendrell, O. & Santra, R. Imaging electronic quantum motion with light. *Proceedings of the National Academy of Sciences* **109**, 11636–11640 (2012). URL http://www.pnas.org/content/109/29/11636.abstract.

[53] Popova-Gorelova, D. & Santra, R. Imaging interatomic electron current in crystals with ultrafast resonant x-ray scattering. *Phys. Rev. B* **92**, 184304 (2015). URL http://link.aps.org/doi/10.1103/PhysRevB.92.184304.

[54] Popova-Gorelova, D., Küpper, J. & Santra, R. Imaging electron dynamics with time- and angle-resolved photoelectron spectroscopy. *Phys. Rev. A* **94**, 013412 (2016). URL https://link.aps.org/doi/10.1103/PhysRevA.94.013412.

[55] Popova-Gorelova, D. Imaging electron dynamics with ultrashort light pulses: A theory perspective. *Applied Sciences* **8**, 318 (2018). URL http://www.mdpi.com/2076-3417/8/3/318.

[56] Taylor, G. The phase problem. *Acta Crystallographica Section D* **59**, 1881–1890 (2003). URL https://doi.org/10.1107/S0907444903017815.

[57] Gonze, X. *et al.* Abinit: First-principles approach to material and nanosystem properties. *Computer Physics Communications* **180**, 2582 – 2615 (2009). URL http://www.sciencedirect.com/science/article/pii/S0010465509002276.

[58] Gonze, X. *et al.* Recent developments in the abinit software package. *Computer Physics Communications* **205**, 106 – 131 (2016). URL http://www.sciencedirect.com/science/article/pii/S0010465516300923.

[59] Gonze, X. *et al.* The abinitproject: Impact, environment and recent developments. *Computer Physics Communications* **248**, 107042 (2020). URL https://www.sciencedirect.com/science/article/pii/S0010465519303741.

[60] Romero, A. H. *et al.* ABINIT: Overview and focus on selected capabilities. *The Journal of Chemical Physics* **152**, 124102 (2020). URL https://doi.org/10.1063/1.5144261.

[61] Perdew, J. P., Burke, K. & Ernzerhof, M. Generalized gradient approximation made simple. *Phys. Rev. Lett.* **77**, 3865–3868 (1996). URL https://link.aps.org/doi/10.1103/PhysRevLett.77.3865.

[62] Hamann, D. R. Optimized norm-conserving vanderbilt pseudopotentials. *Phys. Rev. B* **88**, 085117 (2013). URL https://doi.org/10.1103/physrevb.88.085117.

[63] Levine, Z. H. & Allan, D. C. Linear optical response in silicon and germanium including self-energy effects. *Phys. Rev. Lett.* **63**, 1719–1722 (1989). URL https://link.aps.org/doi/10.1103/PhysRevLett.63.1719.

[64] Calabrese, E. & Fowler, W. B. Electronic energy-band structure of α quartz. *Phys. Rev. B* **18**, 2888–2896 (1978). URL https://link.aps.org/doi/10.1103/PhysRevB.18.2888.

[65] Momma, K. & Izumi, F. *VESTA3* for three-dimensional visualization of crystal, volumetric and morphology data. *Journal of Applied Crystallography* **44**, 1272–1276 (2011). URL http://dx.doi.org/10.1107/S0021889811038970.

Acknowledgment

Daria Popova-Gorelova acknowledges the funding from the Volkswagen Foundation through a Freigeist Fellowship, grant number 96 237. The authors acknowledge support from DESY (Hamburg, Germany), a member of the Helmholtz Association HGF. This work was supported in part by the Deutsche Forschungsgemeinschaft (DFG, German Research Foundation) - 491245950.

Author contributions

D. P.-G. conceived the study and wrote the manuscript. R. S. supervised the study and edited the manuscript.

Competing interests

The authors declare no competing interests.